RESEARCH ARTICLE | DECEMBER 05 2024

Onset of kinetic effects on Rayleigh–Taylor instability: Advective–diffusive asymmetry

Special Collection: K. R. Sreenivasan: A Tribute on the occasion of his 75th Birthday

Swapnil Majumder (स्वप्निल मजूमदार) ; Daniel Livescu ; Sharath S. Girimaji (शरथ गिरिमाजी)

Physics of Fluids 36, 124113 (2024)
https://doi.org/10.1063/5.0240103

Onset of kinetic effects on Rayleigh–Taylor instability: Advective–diffusive asymmetry

Cite as: Phys. Fluids **36**, 124113 (2024); doi: 10.1063/5.0240103
Submitted: 24 September 2024 · Accepted: 13 November 2024 ·
Published Online: 5 December 2024

Swapnil Majumder (स्वप्निल मजूमदार),[1,a)] Daniel Livescu,[2] and Sharath S. Girimaji (शरथ गिरिमाजी)[3]

AFFILIATIONS

[1]Department of Aerospace Engineering, Texas A&M University, College Station, Texas 77843, USA
[2]CCS-2, Los Alamos National Laboratory, Los Alamos, New Mexico 87545, USA
[3]Department of Ocean Engineering, Texas A&M University, College Station, Texas 77843, USA

Note: This paper is part of the special topic, K. R. Sreenivasan: A Tribute on the occasion of his 75th Birthday.
[a)]**Author to whom correspondence should be addressed:** swapnil19@tamu.edu

ABSTRACT

In nature and engineering applications, the Rayleigh–Taylor instability (RTI) occurs over a wide range of Atwood, Reynolds, Mach, and Knudsen numbers. At low Atwood, Mach, and Knudsen numbers, the classic advective instability causes quasi-symmetric bubble and spike growth on the two sides of the interface. However, recent findings suggest that at high degrees of rarefaction, advective effects are suppressed and molecular diffusion leads to planar growth of the density fronts on either side of the interface. This study aims to investigate the flow physics of the transition from advective to diffusive behavior, focusing on the onset of the kinetic effects. Using the gas kinetic methodology, RTI is simulated over a range of Knudsen and Mach numbers in the transition regime. The simulation results reveal the various stages of transformation from advective instability to diffusive transport. For the first time, the study demonstrates the existence of a Knudsen–Mach parameter regime where the bubble side exhibits advective instability, while the other side shows a planar density front due to molecular diffusion, rather than the canonical advective spike shape. The dominance of different mechanisms on the two sides of the interface leads to the advective–diffusive asymmetry. The findings of this study can lead to a more comprehensive understanding of RTI over a wide range of Mach and Knudsen numbers.

I. INTRODUCTION

Rayleigh–Taylor instability (RTI) manifests at the interface between two initially segregated fluids of different densities subject to the influence of an appropriate accelerating force.[1,2] This hydrodynamic instability occurs widely in nature (e.g., atmosphere, ocean systems, and astrophysics) and engineering flows (e.g., inertial confinement fusion, materials processing, multi-phase flows, and combustion systems).[3–6] The RTI is characterized by intricate flow patterns in the proximity of the interface, which lead to increased mixing between the two fluids. At high-density ratios, the classical RTI development is different on the sides, with sharper, more elongated structures on the light fluid side ("spikes") and smoother, more rounded structures on the heavy fluid side ("bubbles"). These structures become increasingly similar at lower density ratios.

The nature of Rayleigh–Taylor instability (RTI), the resulting flow pattern, and the mixing rate are highly influenced by the Atwood, Reynolds, Mach, and Knudsen numbers of the flow. Wei and Livescu[7] outline the various stages of single-mode RTI development at low-density ratios, identifying a chaotic stage in the later phases of RTI growth that depends on reaching a minimum Reynolds number threshold. Bian *et al.*[8] examine the effect of the Reynolds number on fully compressible RTI, finding a threshold perturbation Reynolds number (Re_p) above which the bubble re-accelerates beyond the "terminal velocity" that might occur even at large Atwood numbers. Investigating the effect of compressibility on RTI is more challenging due to multiple influencing factors, including the type of background stratification and multi-fluid effects. Weiland *et al.*[9] study the impact of isothermal stratification on RTI evolution, observing that instability growth saturates as the stratification parameter increases, while Weiland *et al.*[10] found that an isochoric background state leads to increased instability at higher Mach number. Majumder *et al.*[11] further consider the intrinsic compressibility effects of an initial isochoric background state, discovering that increased compressibility leads to enhanced destabilization and greater bubble–spike asymmetry. This destabilization and asymmetry are attributed to a rise in the mean pressure gradient with increasing compressibility, resulting in enhanced baroclinic vorticity generation.

The investigation of the kinetic (non-continuum) effects on the RTI poses further challenges as effects not captured by the Navier–Stokes equations start to play a role. The kinetic effects on flow dynamics can be parameterized in terms of the Knudsen number, *Kn*, which is the ratio of the molecular mean-free path (l) and the characteristic length scale of the flow (L). Sagert *et al.*[12] study the effect of Knudsen number on RTI growth using direct simulation Monte Carlo (DSMC) method. They find that increasing the Knudsen number causes RTI growth to be more diffusive, and at high enough Knudsen numbers, bubbles and spikes do not form. Due to the inherent limitations of DSMC in the low *Kn* regime, Ref. 12 also reports observing certain unphysical features in the transition regime.

Extensive studies have been conducted on RTI in the continuum regime for both incompressible and compressible cases, elucidating insights into canonical bubble and spike growth. However, research on RTI in the rarefied regime is more limited. It has been recently reported that at sufficiently high Knudsen numbers, the typical bubble and spike structures fail to develop.[12] The goal of this study is to examine the onset of kinetic effects on RTI in the transition regime between the classical bubble–spike geometry to planar diffusion front behavior. Toward this end, the paper addresses the following objectives:

1. Identify the appropriate metrics to quantify the advective, diffusive, and pressure effects in the RTI flow.
2. Investigate the transition in the density contours from bubble–spike to planar front shapes.
3. Establish the unique flow characteristics in the *Kn*–*M* transition regime.

In this work, we simulate the single-mode Rayleigh–Taylor instability (RTI) evolution using the gas kinetic method (GKM). GKM uses the Boltzmann equation to calculate the numerical fluxes instead of the traditional Navier–Stokes Equations. It has been established that GKM works well for continuum and transition flows for low Knudsen numbers ($\mathrm{Kn} < 0.01$).[13] Thus, this methodology is ideally suited for examining the transition regime going from continuum to weakly rarefied. In our previous works, we have used GKM to study the onset of transition effects in mixing layers[14] and cavity flows.[15] In future works, we plan to investigate RTI at higher Knudsen numbers using the unified gas kinetic scheme,[16,17] which is valid for high degrees of rarefaction.

The paper is organized as follows. Section II presents the continuum equations and the initial background state. Metrics quantifying the advective, pressure, and diffusive effects are developed. In Sec. III, a brief description of the gas kinetic method (GKM) is given. Validation cases are also presented. The RTI simulation results over a range of *Kn* and *Ma* parameters are presented in Sec. IV. The various regimes of instability and corresponding flow mechanisms are also established. Section V concludes the paper with a summary and major inferences.

II. GOVERNING EQUATIONS

The conservation equations of mass, momentum, and energy are used to identify the metrics for advective, diffusive, and pressure effects, which will be used to discuss the onset of kinetic effects on the Rayleigh—Taylor instability,

$$\frac{\partial \rho^*}{\partial t^*} + \frac{\partial \rho u_j^*}{\partial x_j^*} = 0, \tag{1a}$$

$$\frac{\partial \rho u_i^*}{\partial t^*} + \frac{\partial \rho u_i^* u_j^*}{\partial x_j^*} = -\frac{\partial p^*}{\partial x_i^*} + \rho^* g_i^* + \frac{\partial \sigma_{ij}^*}{\partial x_j^*}, \tag{1b}$$

$$\frac{\partial \rho e^*}{\partial t^*} + \frac{\partial \rho^* e^* u_j^*}{\partial x_j^*} = -\frac{\partial p^* u_i^*}{\partial x_i^*} + \rho u_i^* g_i^* + \frac{\partial \sigma_{ij}^* u_i^*}{\partial x_j^*} - \frac{\partial q_j^*}{\partial x_j^*}. \tag{1c}$$

Under the assumption of ideal gas law, the pressure and total energy can be written as

$$p^* = \rho^* R^* T^*, \tag{1d}$$

$$e^* = \frac{1}{2} u_i^* u_i^* + c_v^* T^*. \tag{1e}$$

The variables with superscript * represent dimensional quantities. Here, ρ^* represents the density of the flow, u_i^* is the velocity of the flow, T^* is the temperature, and p^* is the pressure. $g_i^* = [-g, 0, 0]$ is the gravitational acceleration, and e^* is the total energy of the flow, comprising of kinetic and internal energies. R^* and c_v^* are the specific gas constant and specific heat capacity at constant volume, respectively. The viscous stress tensor (σ_{ij}^*) and heat flux vector (q_j^*) can be represented as follows:

$$\sigma_{ij}^* = 2\mu^* S_{ij}^* - \frac{2}{3}\mu^* \frac{\partial u_k^*}{\partial x_k^*}\delta_{ij}, \quad S_{ij}^* = \frac{1}{2}\left(\frac{\partial u_i^*}{\partial x_j^*} + \frac{\partial u_j^*}{\partial x_i^*}\right), \tag{2}$$

$$q_j^* = -\kappa^* \frac{\partial T^*}{\partial x_j^*}. \tag{3}$$

Here, μ^* and κ^* are the dynamic viscosity and the coefficient of thermal conductivity of the fluid, respectively. δ_{ij} represents the Kronecker delta function. The governing equations are solved for a single-mode RTI with an initial isochoric background state. This corresponds to the initial density profile being constant away from the interface and takes the following form:

$$\rho_0^* = \rho_l^* + 0.5\left[1 + \mathrm{erf}\left(Y_v \frac{x_1^*}{L_{x_1^*}}\right)\right](\rho_h^* - \rho_l^*), \tag{4}$$

where ρ_h^* and ρ_l^* are the high and low densities, respectively. The error function is used for a smooth jump at the interface between the two densities ($x_1 = 0$). Y_v is a parameter controlling the shape of the error function and is set to 34.[8,11] The density and pressure at the interface are given by p_I and ρ_I ($= \frac{\rho_h^* + \rho_l^*}{2}$). The background pressure profile is determined from the initial hydrostatic condition

$$p_0^* = p_I - \rho^* g^* x_1^*. \tag{5}$$

Figure 1 shows the initial background density and pressure profiles. A single mode of perturbation wavelength λ is introduced at the interface. The dimensional variables are normalized as follows:

$$\rho = \frac{\rho^*}{\rho_I}, \quad p = \frac{p^*}{p_I}, \quad T = \frac{p_I}{\rho_I R^*}, \quad u_i = \frac{u_i^*}{\sqrt{Ag\lambda}}, \quad x_i = \frac{x_i^*}{\lambda}, \tag{6}$$

where ρ_I and p_I are the density and pressure at the interface, respectively, and λ is the initial wavelength of the perturbation, and A is the Atwood number defined below. The governing equations are then written in non-dimensional form,

$$\frac{\partial \rho}{\partial t} + \frac{\partial \rho u_j}{\partial x_j} = 0, \tag{7a}$$

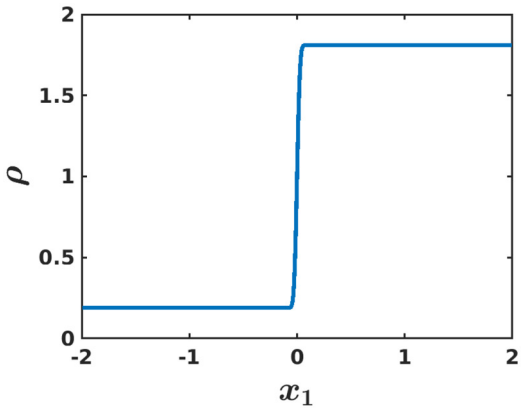

(a) Density profile

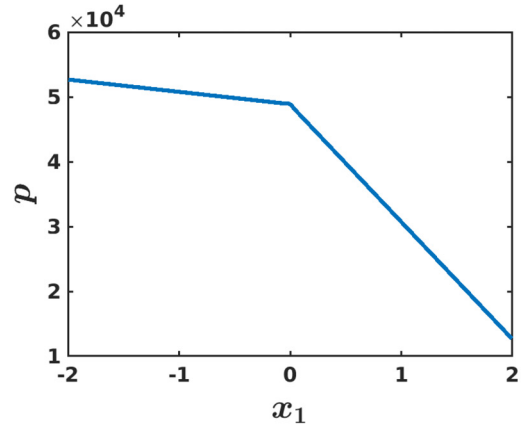

(b) Pressure profile

FIG. 1. Initial background profiles for (a) density and (b) pressure.

$$\frac{\partial \rho u_i}{\partial t} + \frac{\partial \rho u_i u_j}{\partial x_j} = -\frac{1}{AM^2}\frac{\partial p}{\partial x_i} + \frac{1}{Fr^2}\rho g_i + \frac{1}{Re}\frac{\partial \sigma_{ij}}{\partial x_j}, \tag{7b}$$

$$\frac{\partial \rho e}{\partial t} + \frac{\partial \rho e u_j}{\partial x_j} = -\frac{1}{AM^2}\frac{\partial p u_i}{\partial x_i} + \frac{1}{Fr^2}\rho u_i g_i + \frac{1}{Re}\frac{\partial \sigma_{ij} u_i}{\partial x_j} - \frac{\gamma}{(\gamma-1)ARePrM^2}\frac{\partial}{\partial x_j}\left(\kappa \frac{\partial T}{\partial x_j}\right), \tag{7c}$$

$$p = \rho T, \tag{7d}$$

$$e = \frac{1}{2}u_i u_i + \frac{1}{(\gamma-1)AM^2}c_v T. \tag{7e}$$

The viscous stress tensor is defined by

$$\sigma_{ij} = 2\mu S_{ij} - \frac{2}{3}\mu\frac{\partial u_k}{\partial x_k}\delta_{ij}, \quad S_{ij} = \frac{1}{2}\left(\frac{\partial u_i}{\partial x_j} + \frac{\partial u_j}{\partial x_i}\right). \tag{8}$$

Here, $\kappa = \kappa^*/\kappa_r$, $\mu = \mu^*/\mu_r$, and $c_v = c_v^*(\gamma-1)/R^*$ are the non-dimensional heat conduction coefficient, dynamic viscosity, and specific heat at constant volume, respectively, and γ is the ratio of specific heat. Based on the reference quantities, the non-dimensional parameters governing the instability growth are the perturbation Reynolds number, Atwood number, Mach number, Froude number, and Prandtl number,

$$Re = \frac{\rho_I \lambda}{\mu_r}\sqrt{Ag\lambda}, \quad A = \frac{\rho_h^* - \rho_l^*}{\rho_h^* + \rho_l^*}, \quad M = \sqrt{\frac{\rho_I g \lambda}{p_I}}, \quad Fr^2 = \frac{Ag\lambda}{g\lambda} = A, \quad Pr = \frac{\mu_r \gamma R^*}{\kappa_r(\gamma-1)}. \tag{9}$$

The Reynolds number (Re) is based on the length scale λ and gravitational wave speed, $\sqrt{g\lambda}$, as the velocity scale. The Atwood number (A) represents the initial density jump at the interface and is related to the strength of the driving buoyancy force. The Mach number (M) is the ratio between the gravitational wave speed and the isothermal speed of sound. This particular definition of Mach number for RTI stems from the linear analysis of Livescu[18] and represents the static compressibility effects. A perturbation Reynolds number can also be defined as $Re_p = \frac{\rho_I \lambda}{\mu_r}\sqrt{\frac{Ag\lambda}{1+A}}$ based on the terminal velocity from buoyancy-drag models.[7] Since the factor $(1+A)$ is the same for the simulations considered here and does not appear in the other scalings, it was left aside from the discussion in this paper for simplicity. The onset of kinetic effects on RTI is measured using the Knudsen number, which is defined based on the ratio of the wavelength of the initial perturbation (λ) and the molecular mean-free path (l),

$$Kn = l/\lambda. \tag{10}$$

The molecular mean-free path can be related to the kinematic viscosity (ν) and flow speed of sound (c),[19]

$$l = \frac{\nu}{c}\sqrt{\frac{\pi\gamma}{2}}. \tag{11}$$

Taking $\nu = \mu_r/\rho_I$ and $c = \sqrt{\frac{\gamma p_I}{\rho_I}}$, this relationship can be rewritten in terms of the non-dimensional numbers Re, M, and A,

$$Kn = \frac{M\sqrt{A}}{Re}\sqrt{\frac{\pi}{2}}. \tag{12}$$

The Knudsen number typically reflects kinetic effects (or departure from continuum approximation) on a flow. These effects on flow instabilities have been considered on various flow instabilities, including Taylor–Couette flow,[20] Kolmogorov flow,[21] Rayleigh–Benard Flow,[22–24] and Kelvin–Helmholtz instability.[14] These studies demonstrate a stabilization effect of increasing departure from continuum limit on instability growth. Large Kn effects can occur as the molecular mean-free path becomes large (e.g., rarefied flows as encountered in high altitude flight or reentry to the atmosphere). In the context of RTI occurring inside an inertial confinement fusion (ICF) capsule, the kinetic effects manifest through an increase in Knudsen number due to the exceedingly small flow length scale. Nevertheless, both situations fall under the purview of high Knudsen number flows.

III. METHODOLOGY

The foregoing analysis was based on the continuum governing equations. This section elaborates the gas kinetic method (GKM), which is used to perform direct numerical simulations of single-mode

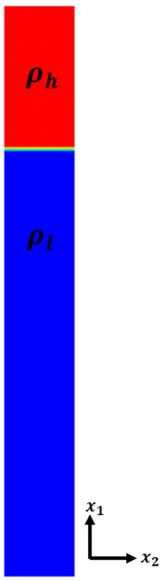

FIG. 2. Computational setup of two-dimensional single-mode RTI. The high-density fluid is denoted by ρ_h and low-density fluid by ρ_l. The domain lengths in the x_1 and x_2 directions are λ and 8λ, respectively.

Rayleigh–Taylor instability.[19,25–27] GKM is a kinetic-based finite volume approach used for solving highly compressible and rarefied non-equilibrium flow problems.

The Boltzmann equation describes the transport of a single-particle distribution function $f(\vec{x}, \vec{c}, t)$

$$\frac{\partial f}{\partial t} + \vec{c} \cdot \nabla f + \vec{a} \cdot \nabla_c f = \frac{g - f}{\tau}, \tag{13}$$

where $\vec{x}$ is the position, $\vec{c}$ is the velocity, $\vec{a}$ is the particle acceleration due to external force, and t is the time. The collision timescale is represented by τ. The function f resides in a six-dimensional phase space comprising three spatial coordinates and three velocity coordinates. The term on the RHS $((\frac{\partial f}{\partial t})_{collisions})$ is modeled using the Bhatnagar–Gross–Krook model[28]), where g is the Maxwellian distribution. The Boltzmann-BGK model is employed in the current method to obtain the numerical fluxes. The details of GKM can be found in Refs. 19, 25, and 26. Here, we highlight the main features. The conservation equation can be cast in a finite volume formulation as follows:

$$\frac{\partial}{\partial t}\int_\Omega U\, dx + \oint_A \vec{F} \cdot d\vec{A} = 0, \tag{14}$$

where the vector U contains the conservation variables $[\rho, \rho u_i, \rho e]$ and F is the flux of the variables U. A fifth-order weighted essential non-oscillatory scheme (WENO)[29] scheme is used to interpolate the cell-centered variables to compute the cell face quantities. The fluxes of the conservative variables are calculated as follows:

$$F_{i+\frac{1}{2}} = [F_\rho, F_{\rho u_i}, F_{\rho e}]^T = \int_{-\infty}^{\infty} c_i \psi f(t, c_i, \xi)\, d\Xi, \tag{15}$$

where the fluxes of the three conserved quantities, mass, momentum, and energy, are given by F_ρ, $F_{\rho u_i}$, and $F_{\rho e}$, respectively. These fluxes

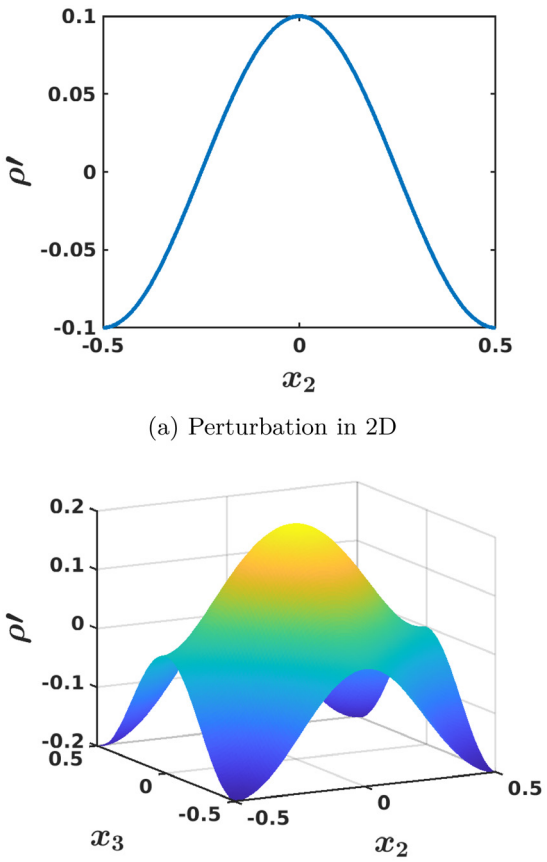

(a) Perturbation in 2D

(b) Perturbation in 3D

FIG. 3. Density perturbation in 2 and 3D.

are calculated as moments of the particle distribution function f. $d\Xi = dc_1 dc_2 dc_3 d\xi$ is an elemental volume in the phase space, where ξ is the internal degrees of freedom. The integration process encompasses velocity coordinates within the phase space as well as all other internal degrees of freedom. Denoting ψ as the vector of moments corresponding to the fluxes of each conserved quantity,

$$\psi = \left(1, c_i, \frac{1}{2}(c_1^2 + c_2^2 + c_3^2 + \xi^2)\right). \tag{16}$$

The B-BGK equation is solved using the method of characteristics to obtain f at the cell interface. After solving for f, we update the macroscopic values at the cell center based on the fluxes as follows:

$$\begin{aligned} U_i^{n+1} = U_i^n &- \frac{1}{\Delta x}\int_t^{t+\nabla t} (F_{i+1/2}(t) - F_{i-1/2}(t))\, dt \\ &- \frac{1}{\Delta y}\int_t^{t+\nabla t} (G_{i+1/2}(t) - G_{i-1/2}(t))\, dt \\ &- \frac{1}{\Delta z}\int_t^{t+\nabla t} (H_{i+1/2}(t) - H_{i-1/2}(t))\, dt. \end{aligned} \tag{17}$$

TABLE I. List of parameters for the simulations considered in this study. All simulations have $A = 0.8$.

Kn	M	Re	Dominant bubble side growth mechanism	Dominant spike side growth mechanism
Two-dimensional simulation				
	0.35	255.06	Advective	Advective
0.002	0.2	145.71	Advective	Advective
	0.1	72.81	Advective	Advective
	0.35	102.03	Advective	Advective
0.005	0.2	58.30	Advective	Advective
	0.1	29.15	Diffusive	Diffusive
	0.35	72.88	Advective	Advective
0.007	0.2	41.64	Advective	Diffusive
	0.1	20.81	Diffusive	Diffusive
	0.35	51.01	Advective	Advective
0.01	0.2	29.15	Diffusive	Diffusive
	0.1	14.57	Diffusive	Diffusive
	0.35	40.41	Advective	Diffusive
0.0126	0.2	23.13	Diffusive	Diffusive
	0.1	11.55	Diffusive	Diffusive
Three-dimensional simulation				
0.007	0.2	41.64	Advective	Diffusive
0.0126	0.35	40.41	Advective	Diffusive

A. Computational setup

The computational domain describing the setup for the numerical simulations is shown in Fig. 2. The high-density fluid (ρ_h) is positioned above the low-density fluid (ρ_l). A single-mode perturbation is given at the interface between the two fluids. For two-dimensional cases, the perturbation takes the following form, with wavelength λ:

$$\rho' = B\cos\left(\frac{2\pi x_2}{\lambda}\right). \tag{18}$$

Similarly, for three-dimensional cases, the density perturbation can be written as

$$\rho' = B\left[\cos\left(\frac{2\pi x_2}{\lambda}\right) + \cos\left(\frac{2\pi x_3}{\lambda}\right)\right]. \tag{19}$$

B is the amplitude of the perturbation. Figure 3 shows the shape of the density perturbation in two and three dimensions. Periodic boundary conditions are applied in the horizontal directions. Navier–Stokes characteristics boundary conditions are applied in the vertical directions to treat the acoustic waves traveling away from the domain properly.[30,31] Table I gives the range of non-dimensional numbers chosen for the simulations presented here. All simulations have $A = 0.8$. Different Mach numbers are achieved by changing the pressure at the interface (p_I). Different Knudsen numbers are achieved by changing the kinematic viscosity, which corresponds to a change in the molecular mean-free path. This specific range of Knudsen and Mach numbers is chosen to encompass the continuum to the onset of the kinetic regime.

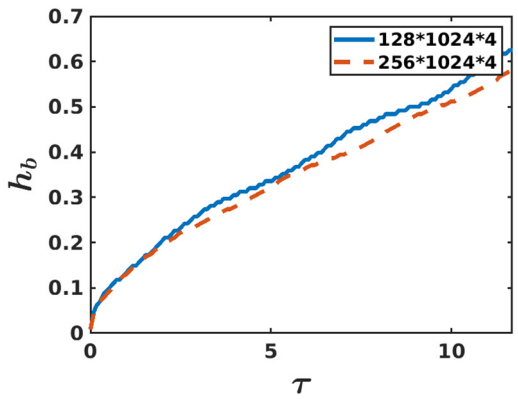

(a) Bubble height

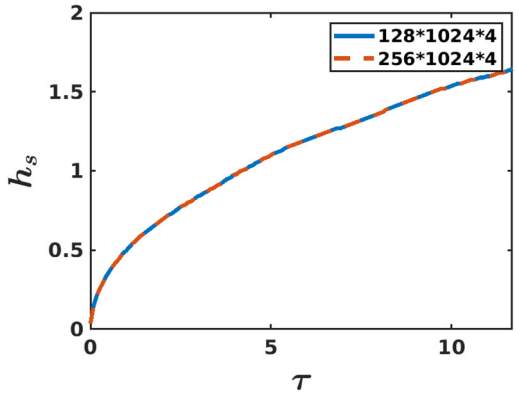

(b) Spike height

FIG. 4. Convergence study for bubble and spike heights at $Kn = 0.0126$, $M = 0.35$, and $A = 0.8$.

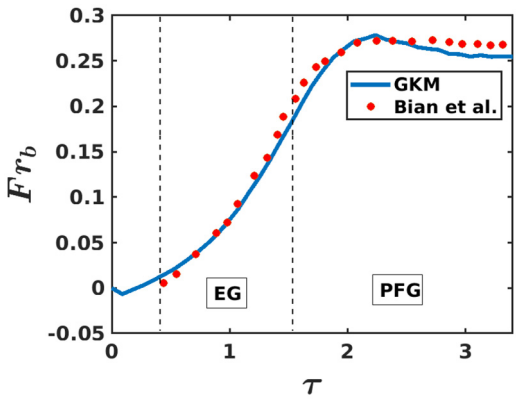

(a) Bubble height

FIG. 5. Comparison of the evolution of bubble speed with Bian *et al.*,[8] for $Re_p = 1000$, $M = 0.0855$, and $A = 0.8$.

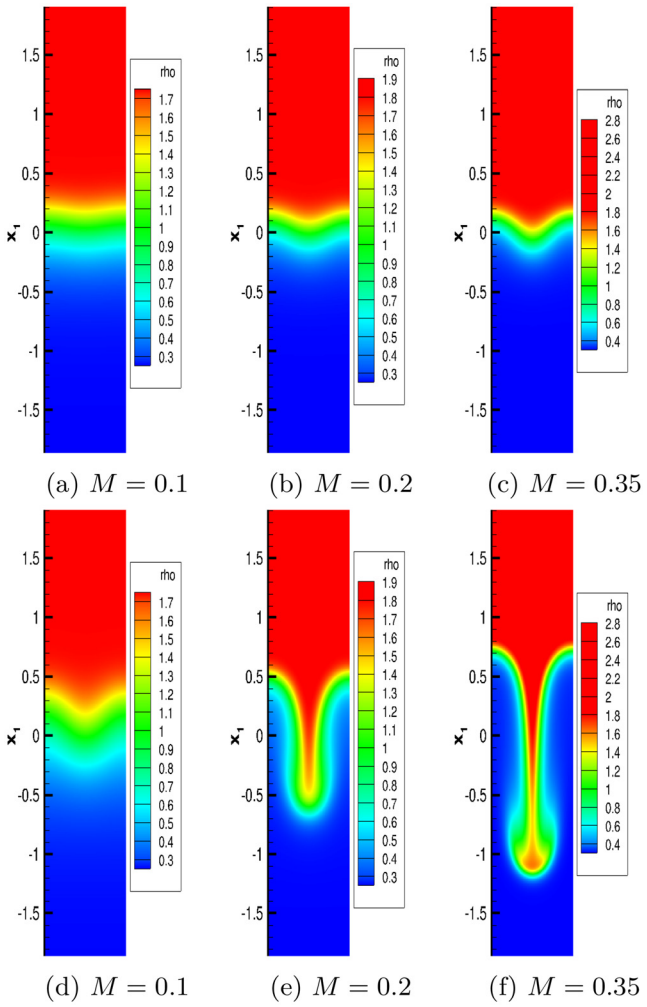

FIG. 6. Density contours are shown for cases with $Kn = 0.002$ at two different times: $\tau = 2.25$ in (a)–(c) and $\tau = 4.5$ in (d)–(e).

A comprehensive convergence and validation study was done by Majumder *et al.*[11] at low Atwood number. Here, we provide additional convergence and validation results for a higher Atwood number ($A = 0.8$). Figure 4 shows the bubble and spike heights for two different mesh sizes. While the bubble height shows some minor differences between the two grids, the spike height essentially overlaps. Consequently, grid resolutions of 128*1024*4 and 128*128*1024 points have been used to perform the two- and three-dimensional simulations, respectively. Figure 5 shows the comparison between bubble speed evolution in the current work with Bian *et al.*[8] It is seen the bubble growth is well captured in the exponential growth region, and well into the potential flow growth zone.

IV. KINETIC AND COMPRESSIBILITY EFFECTS

This section discusses the influence of Knudsen and Mach numbers on the growth of RTI at the onset of kinetic effects. Based on the Knudsen number, RTI growth is categorized into three regimes: advective, diffusive, and intermediate (or advection–diffusion).

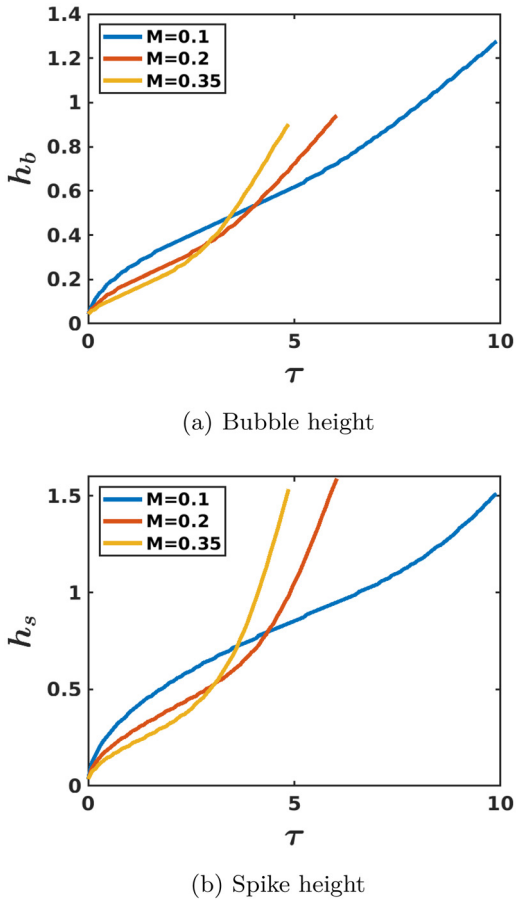

FIG. 7. Evolutions of bubble and spike heights at $Kn = 0.002$ and different Mach numbers.

A. Flow mechanisms

The momentum equation in the vertical direction is analyzed to elucidate the fundamental flow mechanism underlying the onset of RTI growth. The momentum equation is written from Eq. (7b) in the vertical direction ($i = 1$),

$$\frac{\partial \rho u_1}{\partial t} + \frac{\partial \rho u_1 u_j}{\partial x_j} = \frac{1}{\gamma A M^2}\frac{\partial p}{\partial x_1} - \frac{1}{Fr^2}\rho + \frac{Kn}{M\sqrt{A}}\sqrt{\frac{2}{\pi}}\frac{\partial \sigma_{1j}}{\partial x_j}. \tag{20}$$

This equation can be rewritten in non-conservative form as

$$\frac{\partial u_1}{\partial t} = \underbrace{-u_2\frac{\partial u_1}{\partial x_2} - u_1\frac{\partial u_1}{\partial x_1}}_{advection} \underbrace{-\frac{1}{\rho}\frac{1}{\gamma A M^2}\frac{\partial p}{\partial x_1} - \frac{1}{Fr^2}}_{pressure} + \underbrace{\frac{Kn}{M\sqrt{A}}\sqrt{\frac{2}{\pi}}\frac{\sigma}{\rho}}_{viscous}, \tag{21}$$

where σ is the stress in the vertical direction given by

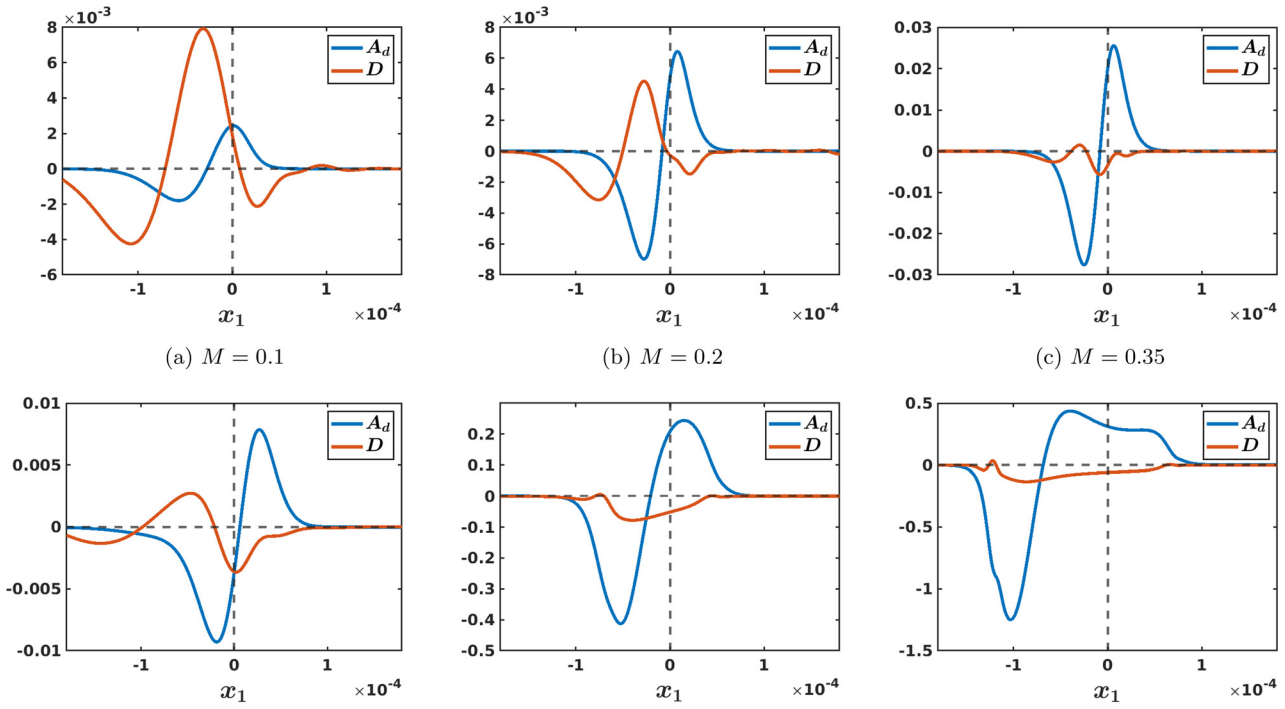

FIG. 8. Evolution of mixing layer width at $Kn = 0.002$ for different Mach numbers.

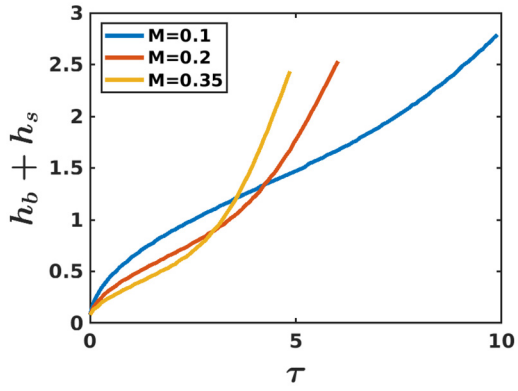

FIG. 9. Comparisons of fundamental physical processes [Eqs. (27) and (29)] for $Kn = 0.002$ at times: $\tau = 2.25$ in (a)–(c) and $\tau = 4.5$ in (d)–(e).

$$\sigma = \left(\frac{\partial^2 u_1}{\partial x_2 \partial x_2} + \frac{1}{3}\frac{\partial^2 u_2}{\partial x_2 \partial x_1} + \frac{4}{3}\frac{\partial^2 u_1}{\partial x_1 \partial x_1}\right). \tag{22}$$

As demonstrated by Eqs. (20)–(22), the transport of momentum depends on three fundamental flow mechanisms: advection, pressure, and viscous action. These processes are explicitly written as follows:

$$A_d(x_1, x_2, t) = \left(-u_2\frac{\partial u_1}{\partial x_2} - u_1\frac{\partial u_1}{\partial x_1}\right), \tag{23}$$

$$P(x_1, x_2, t) = \left(-\frac{1}{\rho}\frac{1}{\gamma A M^2}\frac{\partial p}{\partial x_1} - \frac{1}{Fr^2}\right), \tag{24}$$

$$D(x_1, x_2, t) = \frac{Kn}{M\sqrt{A}}\sqrt{\frac{2}{\pi}}\left(\frac{\sigma}{\rho}\right) dt = \frac{1}{\mathcal{T}}\frac{1}{Re}\int_0^{\mathcal{T}}\left(\frac{\sigma}{\rho}\right). \tag{25}$$

Equation (25) shows that increasing Re has decreases the magnitude of the viscous stress. Additionally, increasing Mach number inhibits diffusive action for a given Knudsen number. The fundamental processes are compared based on spatial averaging in the periodic directions,

$$\langle \mathcal{T} \rangle(x_1, t) = \frac{1}{\lambda}\int_{-\lambda/2}^{\lambda/2} \mathcal{T}(x_1, x_2, t)\, dx_2, \tag{26}$$

where $\langle \mathcal{T} \rangle$ represents the average of a quantity $\mathcal{T}$. These averages can be written for advective, diffusive, and pressure terms as follows:

$$\langle A_d \rangle(x_1, t) = \frac{1}{\lambda}\int_{-\lambda/2}^{\lambda/2} A_d(x_1, x_2, t)\, dx_2, \tag{27}$$

$$\langle P \rangle(x_1, t) = \frac{1}{\lambda}\int_{-\lambda/2}^{\lambda/2} P(x_1, x_2, t)\, dx_2, \tag{28}$$

$$\langle D \rangle(x_1, t) = \frac{1}{\lambda}\int_{-\lambda/2}^{\lambda/2} D(x_1, x_2, t)\, dx_2. \tag{29}$$

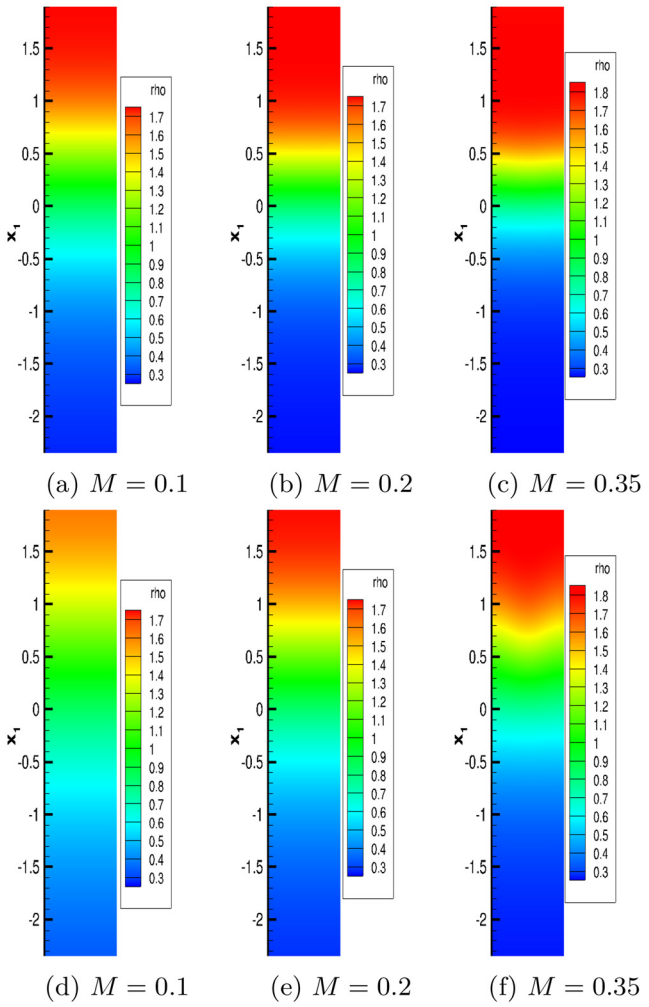

FIG. 10. Density contours are shown for cases with $Kn = 0.0126$ at two different times: $\tau = 4.5$ in (a)–(c), $\tau = 11.7$ in (d)–(f).

To assess a cumulative effect of these processes over time, corresponding integral quantities are also listed as follows:

$$\langle A_d^i \rangle(x_1, \mathcal{T}) = \frac{1}{\lambda}\int_{-\lambda/2}^{\lambda/2}\frac{1}{\mathcal{T}}\int_0^{\mathcal{T}} A_d\, dt\, dx_2, \tag{30}$$

$$\langle P^i \rangle(x_1, \mathcal{T}) = \frac{1}{\lambda}\int_{-\lambda/2}^{\lambda/2}\frac{1}{\mathcal{T}}\int_0^{\mathcal{T}} P\, dt\, dx_2, \tag{31}$$

$$\langle D^i \rangle(x_1, \mathcal{T}) = \frac{1}{\lambda}\int_{-\lambda/2}^{\lambda/2}\frac{1}{\mathcal{T}}\int_0^{\mathcal{T}} D\, dt\, dx_2. \tag{32}$$

Several metrics have been used in previous studies to quantify the growth of bubble and spike heights. These include the location of the maximum density gradient along the bubble/spike axis,[8,11] location of 1% and 5% of mean density values.[9,32] For this study, the 5% thickness definition is chosen as it proves to be the most robust across all the regimes considered in this paper.

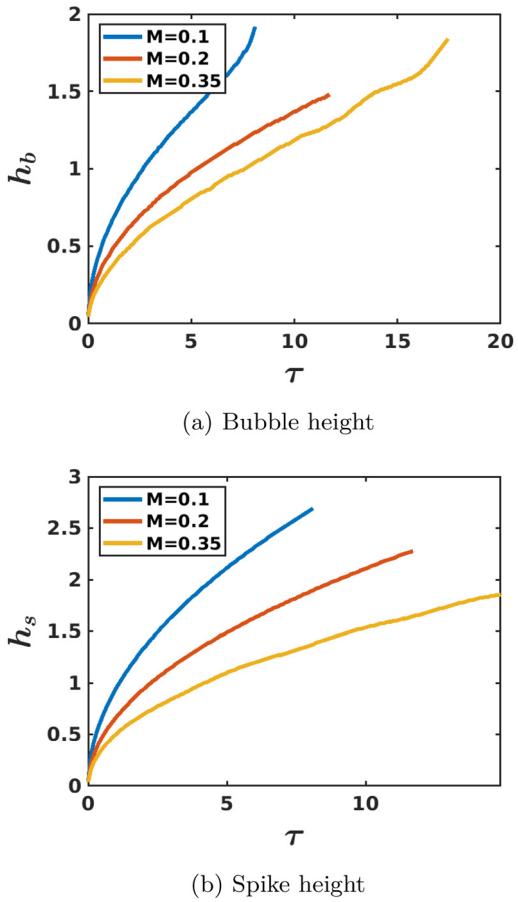

FIG. 11. Evolution of bubble and spike heights for $Kn = 0.0126$ for different Mach numbers.

B. Advective regime

Figure 6 shows the density contours for different Mach numbers. Canonical RTI occurs on both the bubble and spike sides in this regime. An initial diffusive stage is evident at lower Mach numbers (low *Re*). With higher Mach numbers, inertial effects occur faster, resulting in faster development of bubble–spike growth. The bubble–spike asymmetry becomes more pronounced with increasing Mach number, particularly evident for $M = 0.35$, where the spike has descended almost twice the distance than the bubble has.

The evolutions of bubble and spike heights are depicted in Fig. 7 for $Kn = 0.002$. The destabilizing nature of compressibility, at this *Kn* value, can be seen in these figures. An increase in bubble–spike asymmetry is also exhibited with increasing Mach number. For the lowest Mach number, the distances descended (ascended) by the spike (bubble) are almost similar by $\tau = 6$. Meanwhile, for the highest Mach number, spike descension is seen to be greater than bubble ascension.

In Sec. IV A, different flow mechanisms describing the transfer of momentum in the vertical direction were described. Equation 25 indicates a decrease in viscous diffusion with increasing Mach number for

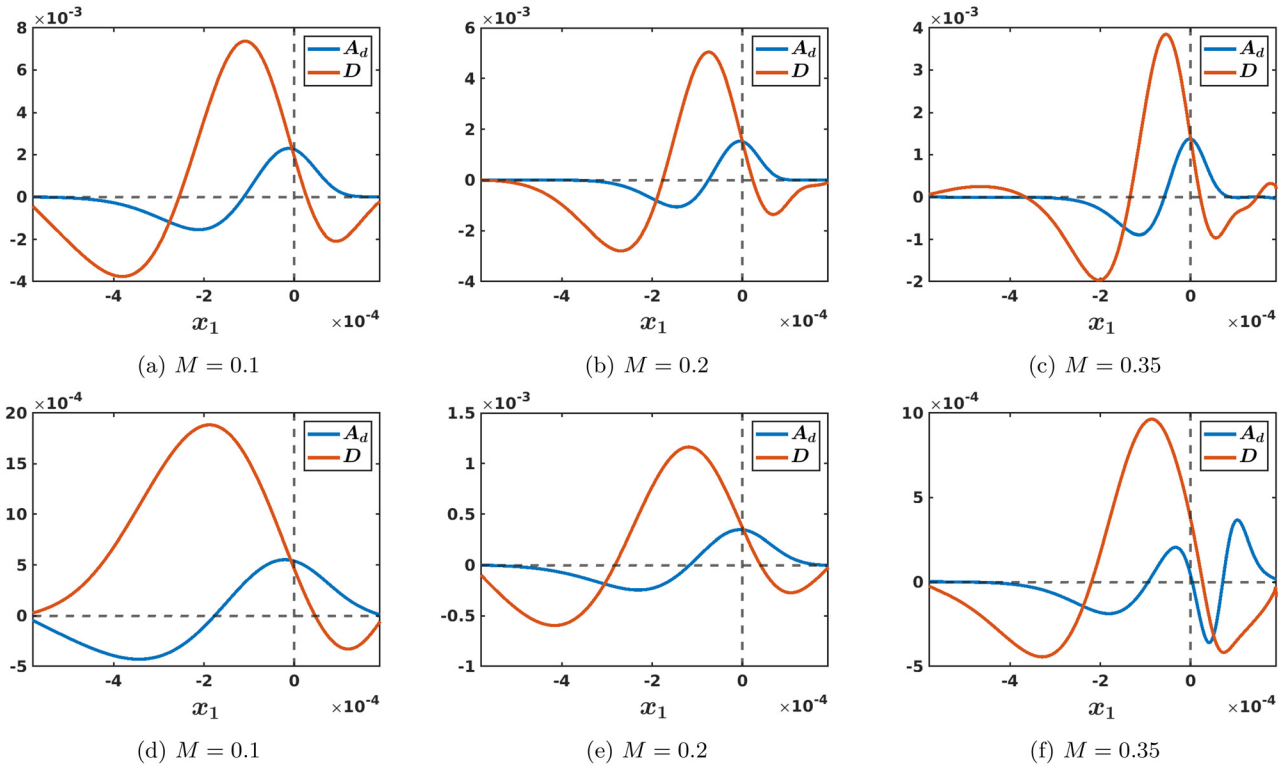

FIG. 12. Evolution of mixing layer width heights for $Kn = 0.0126$ for different Mach numbers.

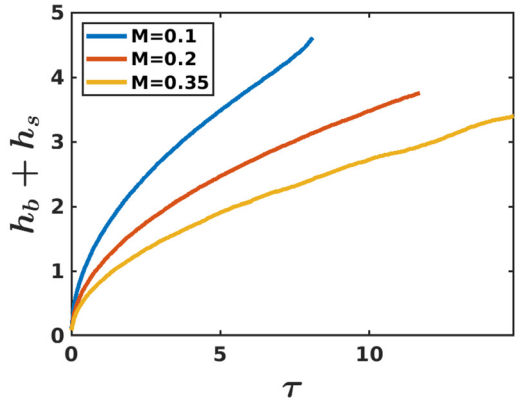

FIG. 13. Comparisons of fundamental physical processes [Eqs. (27) and (29)] for $Kn = 0.0126$ at times: $\tau = 4.5$ in (a)–(c) and $\tau = 11.7$ in (d)–(f).

a given Knudsen number. Here, the profiles of the individual mechanisms are shown to portray the effect of Mach number. Figure 8 delineates the particular mechanisms involved. At early time ($\tau = 2.25$), the effect of viscous diffusion is seen to decrease with increasing Mach number (Reynolds number). The diffusion process exhibits an asymmetric effect, with a greater influence observed on the spike side than on the bubble side. This asymmetry arises due to the presence of density in the denominator on the right hand side of Eq. (25). Thus, the low-density side of the instability occurs on the spike side, while the density is larger on the bubble side, changing the relative magnitude of the viscous term. The decrease in diffusive effects is accompanied by a rise in advective effect as the Mach number increases. At a late time ($\tau = 4.5$), the effect of viscous diffusion drastically decreases with increasing Mach number. Advection dominates over diffusion at all Mach numbers, sustaining canonical instability on both the bubble and spike sides. Figure 9 summarizes the effect of compressibility on the total growth of the mixing layer (bubble plus spike heights). An increase in the mixing layer width is observed with increasing compressibility.

In summary, at $Kn = 0.002$, it is seen that canonical instability growth occurs, with typical bubble and spike development. Compressibility has a twofold effect: an increase in advective processes, which is in corroboration with Majumder *et al.*[11] and a corresponding decrease in diffusive action, as seen from Eq. (25) where the Mach number appears in the denominator of the viscous term.

C. Diffusive regime

At larger Knudsen numbers, the instability lies in the diffusive regime, as can be seen in the density contours shown in Fig. 10 for $Kn = 0.0126$. Two types of instability growth are observed at low and high Mach numbers. At initial times, similar to previous regimes, an initial diffusive phase is evident for all three Mach numbers. The rate of diffusion decreases with increasing Mach number. At later times, for the lowest Mach number, both the bubble and spike sides continue

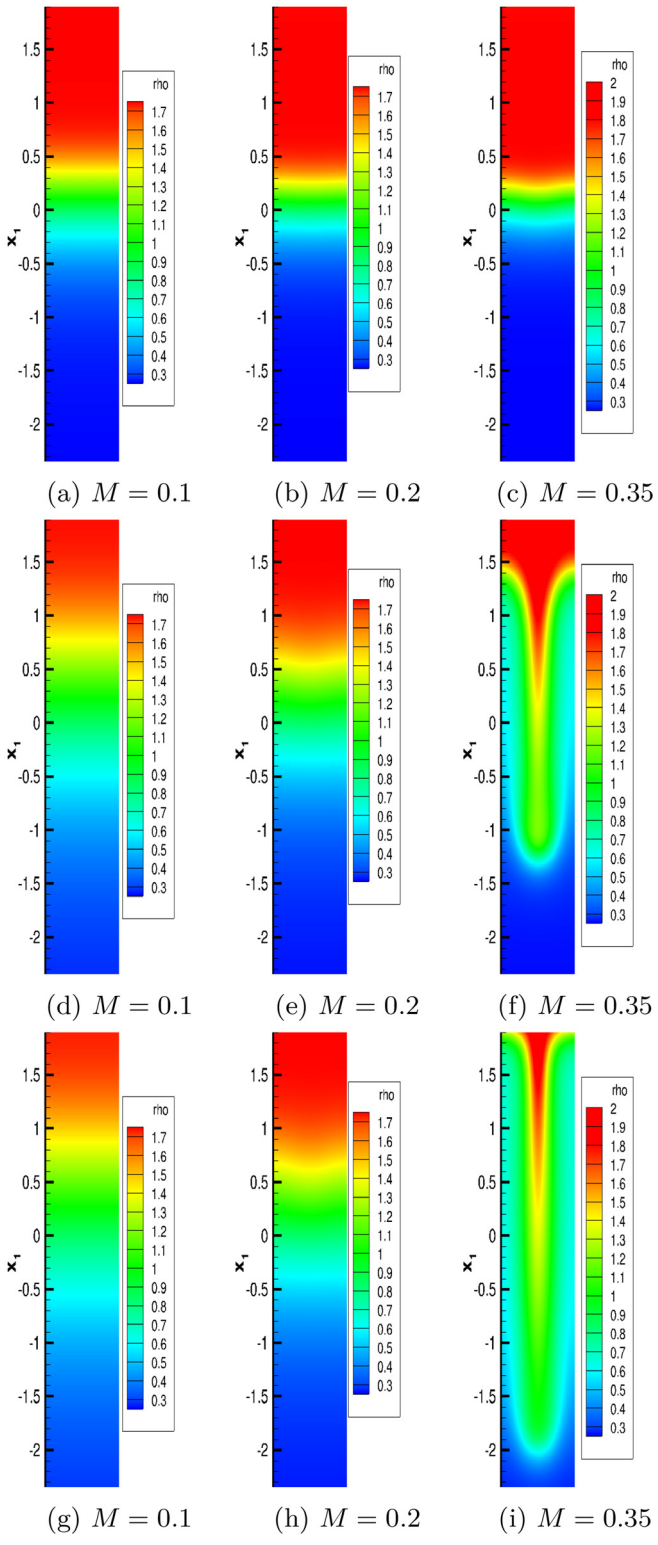

FIG. 14. Density contours are shown for cases with $Kn = 0.007$ at three different times: $\tau = 2.25$ in (a)–(c), $\tau = 9.9$ in (d)–(f), and $\tau = 12.6$ in (g)–(i).

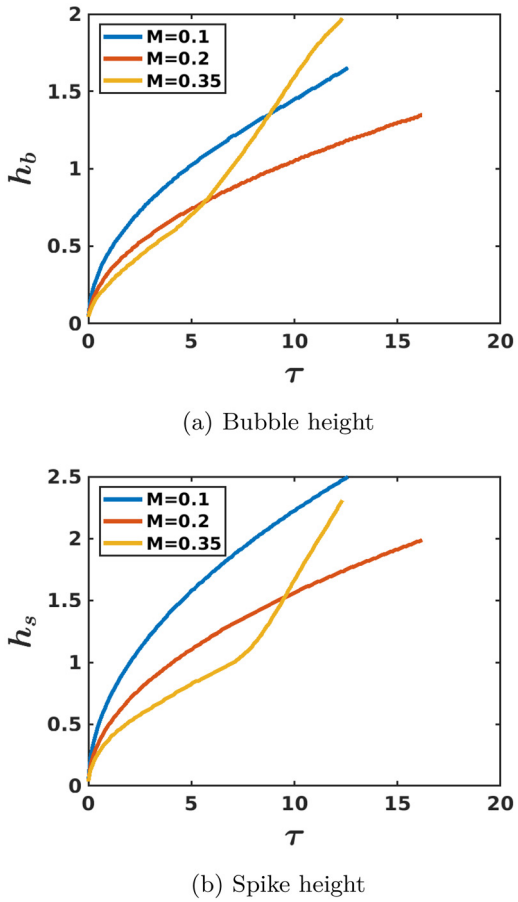

FIG. 15. Evolution of bubble and spike height for Kn = 0.007 at different Mach numbers.

to show pure diffusion. The diffusion occurs asymmetrically, with the spike side showing greater diffusive mixing than the bubble side. The spike side continues to diffuse for higher Mach numbers, although less prominently than for $M = 0.1$. The bubble side begins to show advective growth at higher M values.

Figure 11 shows the bubble spike heights for $Kn = 0.0126$. Both bubble and spike growths diminish with increasing Mach number (or increasing Reynolds number). The bubble–spike asymmetry in diffusion growth is evident. The spike is seen to diffuse almost twice the length of what the bubble diffuses. Figure 12 compares the advective and diffusive processes defined by Eqs. (27) and (29) at this Knudsen number. At an earlier time, the diffusive process surpasses the advective process for both the bubble and spike sides. At later times, the advective process begins to increase its contribution, at a higher rate for higher Mach numbers. Viscous diffusion still dominates over advective processes on the spike side for all Mach numbers. The increase in advection contribution on the bubble side causes canonical bubble growth at higher Mach numbers. Figure 13 summarizes the Mach number effect on the total layer width growth (bubble plus spike) and shows that in the diffusive regime, mixing layer growth decreases with compressibility.

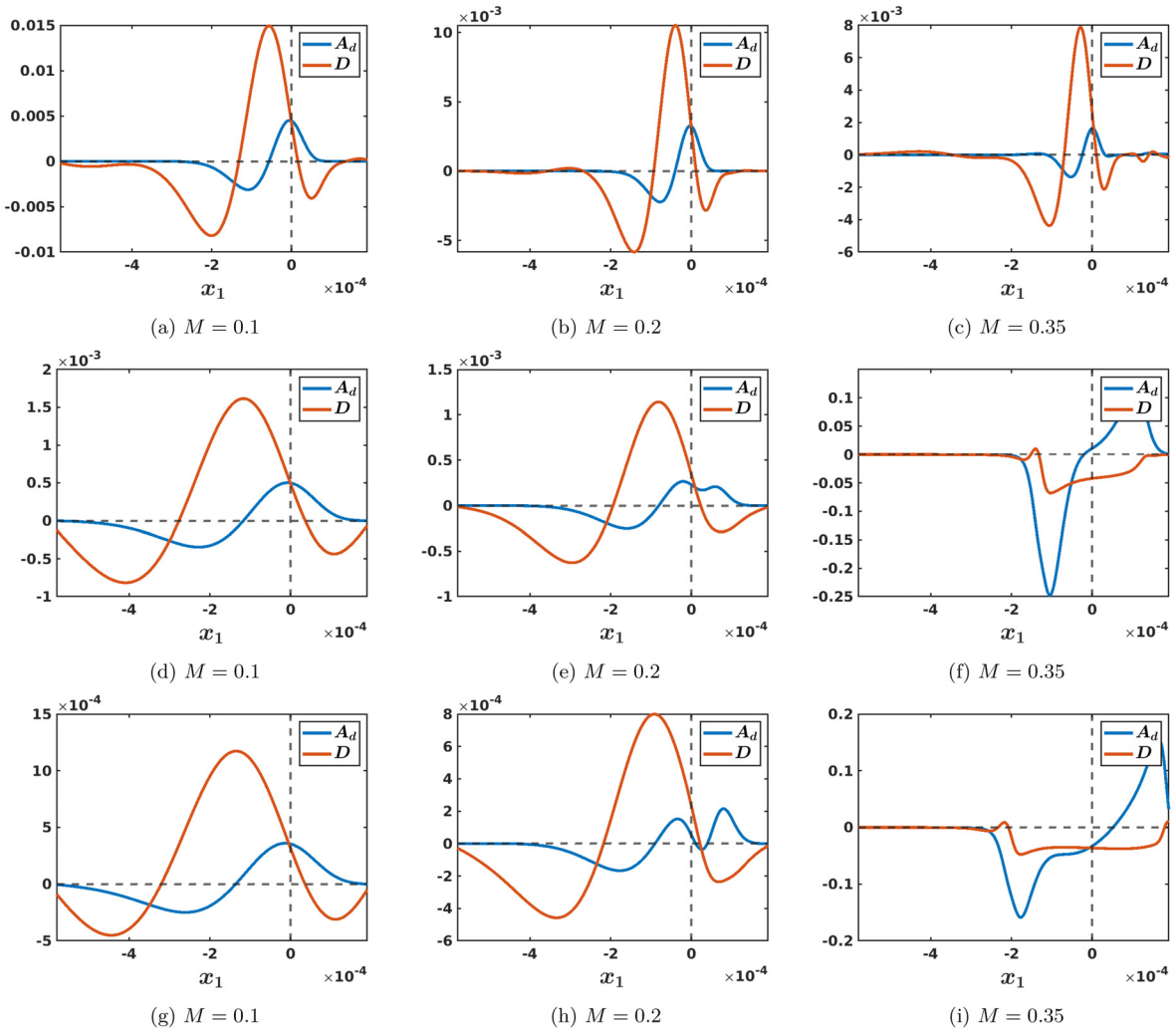

FIG. 16. Evolution of mixing layer width for Kn = 0.007 at different Mach numbers.

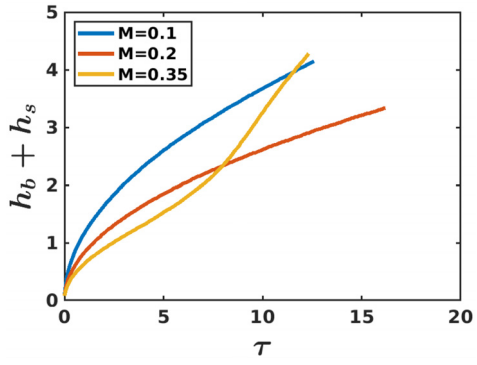

FIG. 17. Comparisons of fundamental physical processes [Eqs. (27) and (29)] for $Kn = 0.007$ at times: $\tau = 2.25$ in (a)–(c), $\tau = 9.9$ in (d)–(f), and $\tau = 12.6$ in (g)–(i).

In summary, at $Kn = 0.0126$, a departure from canonical bubble–spike growth is seen. The two-fronts take on planar shapes, departing from the typical bubble–spike shapes in the canonical RTI. It can be inferred from Eq. (21) that with increasing Knudsen number, the influence of viscous diffusion escalates. The domination of the diffusive transport over advective growth results in planar, rather than bubble–spike fronts.

D. Advective–diffusive regime

Figure 14 presents the density contours for $Kn = 0.007$. Three different kinds of instability growth are observed at different Mach numbers. At the lowest Mach number, both the bubble and spike side exhibit diffusive growth. The spike side demonstrates a more pronounced diffusive character, as identified by its less defined front compared to the bubble side. Consequently, mixing at the spike front is more than at the bubble front. For the intermediate Mach number,

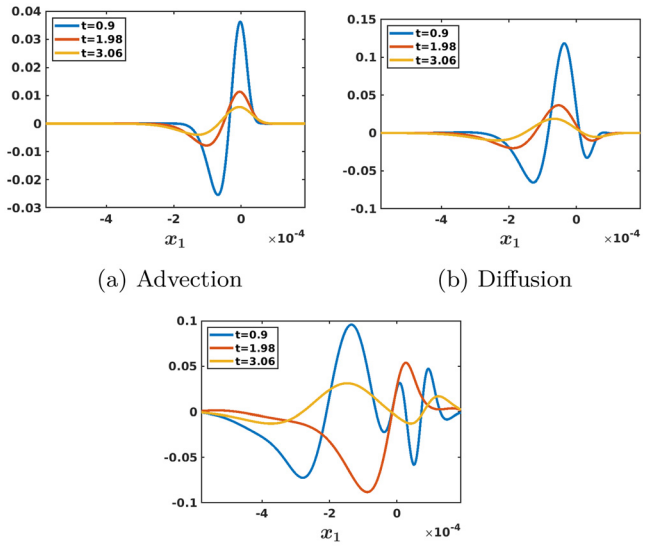

(a) Advection (b) Diffusion

(c) Pressure

FIG. 18. Evolution of instantaneous profiles [Eqs. (27)–(29)] of the fundamental processes for $Kn = 0.0126$ and $M = 0.1$.

initial diffusive growth is observed on both the bubble and spike sides. At a later time, the spike side continues to show diffusive growth, but the bubble front begins to develop a canonical instability shape. For the highest Mach number, an initial diffusive zone is evident, followed by the development of canonical instability on both the bubble and spike sides at later times.

The evolution of bubble and spike heights at different Mach numbers is depicted in Fig. 15. In the initial diffusive phase, increasing

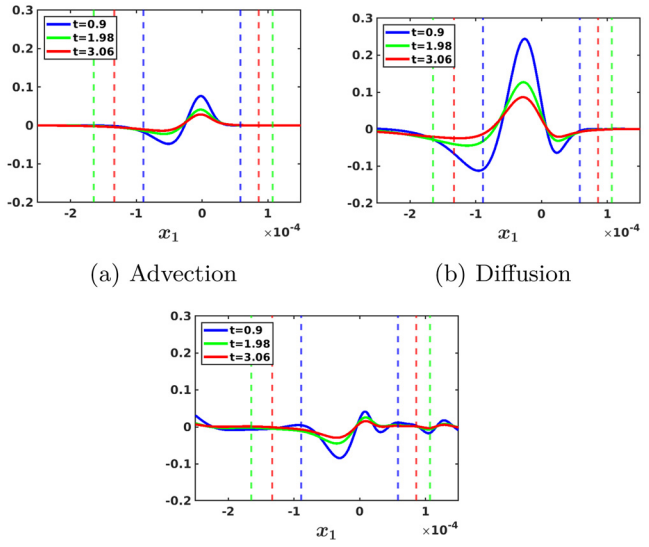

(a) Advection (b) Diffusion

(c) Pressure

FIG. 19. Evolution of integral [Eqs. (30)–(32)] profiles of the fundamental processes for $Kn = 0.0126$.

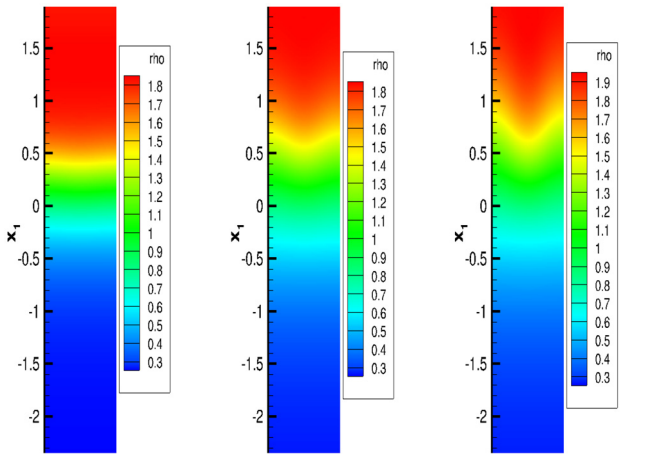

(a) $\tau = 4.5$ (b) $\tau = 11.7$ (c) $\tau = 14.85$

FIG. 20. Density contours are shown for cases with $Kn = 0.0126$ and $M = 0.35$ at a planar location $x_2 = \lambda/4$ in (a)–(c).

the Mach number (corresponding to decreasing the Reynolds number) reduces diffusive growth for both the bubble and the spike sides. The length diffused by the spike side is also more than that of the bubble side, corresponding to the bubble–spike asymmetry identified earlier in the diffusive regime. At later times, for the highest Mach number, a sharp increase in bubble and spike growth is seen compared to the diffusive growth. The canonical growth appears earlier on the bubble side than on the spike side.

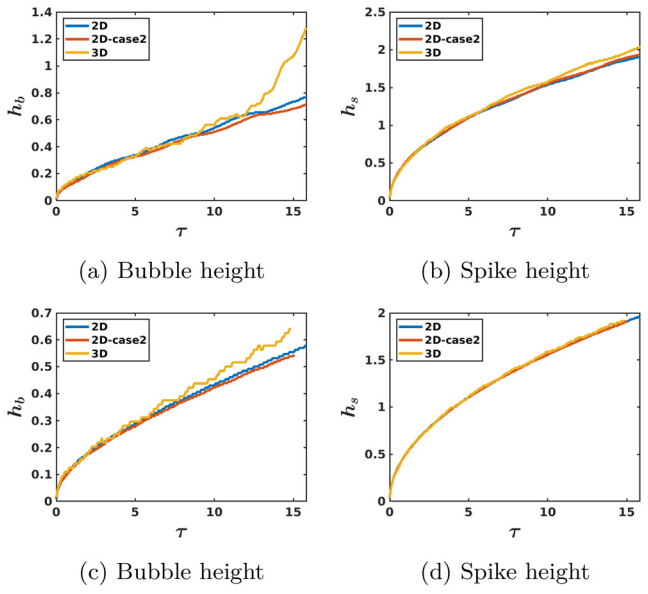

(a) Bubble height (b) Spike height

(c) Bubble height (d) Spike height

FIG. 21. Comparison between the evolution of bubble and spike heights ($h_b = \frac{h_b^*}{\lambda}, h_s = \frac{h_s^*}{\lambda}$, where $*$ quantities are dimensional) for two- and three-dimensional RTI for (a) and (b) $Kn = 0.0126$ and $M = 0.35$ and in (c) and (d) $Kn = 0.007$ and $M = 0.2$.

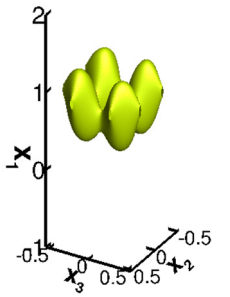

(a) Isosurafce of vorticity magnitude for $\Omega = 14.67$ (70% of Ω_{max})

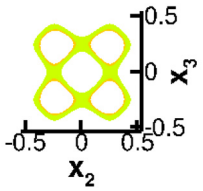

(b) Vorticity magnitude $(14 < \Omega < 15)$ in $x_2 - x_3$ plane at $x_1 = 0.6$

FIG. 22. Vortex ring in 3D RTI at $\tau = 14.85$.

The profiles of the advective and diffusive contributions defined in Eqs. (27) and (29) are shown in Fig. 16. At early times, viscous diffusion dominates over advection on both the spike and bubble side, corresponding to initial diffusive growth. The effect of viscous diffusion is more prominent on the spike side, with the magnitude of the peak decreasing with increasing Mach number. At intermediate times, three different trends for the profiles are observed. For low Mach numbers, viscous effects continue to prevail over advective effects on both sides. The difference is more prominent on the spike side, enhancing diffusive growth. Intermediate Mach numbers show a slight increase in advection on the bubble side, indicating the onset of instability growth. Viscous diffusion is dominating on the spike side. For the highest Mach number, advective processes take a dominant role on both sides. At later times, for the intermediate Mach number, advection dominates over diffusion on the bubble side only. Figure 17 shows the evolution of the total mixing layer width (bubble plus spike) at different Mach numbers. In the low Mach number regime ($M < 0.2$), the mixing-layer width decreases with increasing M. At higher Mach numbers ($M = 0.35$), the mixing layer grows slowly initially under the influence of diffusion. However, at later times, the instability manifests and the mixing-layer growth is rapid surpassing lower Mach number evolution rates.

In summary, at $Kn = 0.007$, the bubble side exhibits canonical advective growth, whereas the spike side evolution is diffusion-dominated resulting in a planar density front. This asymmetric behavior can be understood from examining Eq. (21), wherein the density appearing in the denominator of the viscous term changes the relative importance of diffusive compared to advective effects. Thus, on the spike side, the lower density leads to the dominance of diffusive effects, while on the bubble side, the higher density makes diffusive transport being less influential than advective effects.

E. Role of pressure

We now examine the role of pressure. Figure 18 illustrates the profiles of advection, diffusion, and pressure processes [Eqs. (27)–(29)] at early times. At each instant of time, the magnitude of the pressure-term appears comparable to inertial and viscous effects. It is also evident that, at a given x_1 location, the pressure-term exhibits wavelike behavior. To examine the cumulative effect of pressure over time, the integral quantities [Eqs. (30)–(32)] are shown in Fig. 19. The figures clearly show that the cumulative pressure contribution decreases most rapidly, and has the least effect on the evolution of the density fronts. A thorough examination of other cases confirm that the nature of the late time evolution of the density fronts (at high Mach and Knudsen numbers) is determined by the competition between advective and diffusive effects, with pressure plays a minimal role.

V. THREE-DIMENSIONAL EFFECTS

To understand if the advective–diffusive regime identified above is restricted to the two-dimensional case, the role of kinetic effects on three-dimensional RTI is examined in this section with the same Knudsen number as in Sec. IV D. A comparison is also made with two-dimensional simulations with the same effective wavelength as the three-dimensional ones. The density perturbation for these cases is represented by

$$\rho' = B\cos\left(\frac{2\pi x_2}{\sqrt{2}\lambda}\right). \tag{33}$$

Figure 20 shows the density contours for three-dimensional RTI at similar times and at the highest Mach number considered in Sec. IV D, where the advective diffusive regime is identified. Similarly to the two-dimensional case, the spike side is seen to have a planar front, hence exhibiting diffusive growth. The bubble side, however, is initially diffusive but becomes advective at later times. Hence, the advective–diffusive asymmetry seen in the two-dimensional cases is carried over to three dimensions as well. This demonstrates the similarity of instability dynamics in two and three dimensions for the problem considered here.

Figure 21 compares the bubble and spike height evolution for two-dimensional and three-dimensional cases for two different sets of M–Kn values in the advective–diffusive regime. The growth rate on the spike side is similar in two and three dimensions, portraying the universality of diffusive growth regardless of dimension. On the bubble side, initial diffusive growth coincides, but at later times, advective growth in three dimensions surpasses that in two dimensions. This effect remains even if the effective wavelength between two and three dimensions is the same. Hence, the increase in growth rate for three-dimensional bubble growth is attributed to dissimilar vortex structures in 2 and 3D. For example, Fig. 22 portrays vortex ring formation in 3D RTI. At the same time, Fig. 22(a) shows the isosurface of vorticity magnitude in the 3D RTI case, which resembles a vortex ring. It is well known from potential theory that vortex rings self-propagate faster than vortex pairs, which provides an intuitive explanation for the faster growth seen in Fig. 21 for 3D RTI bubble side compared to 2 D RTI.

VI. SUMMARY AND CONCLUSION

This paper seeks to bridge the knowledge gap regarding the behavior of the interfacial Rayleigh–Taylor instability (RTI) in the

transitional regime between continuum and rarefied flows. The classical RTI featuring bubble and spike structures occurs in the low Mach number continuum regime. This canonical RTI has been well investigated in the literature with experimental and computational studies. Recently, it was shown using DSMC simulations that the bubble–spike structures are suppressed at high degrees of rarefaction. Instead, the density contours propagate on either side of the interface as planar diffusion fronts. In this work we establish, for the first time, the existence of an intermediate Knudsen–Reynolds number parameter regime in which the flow exhibits a mixed behavior. The bubble side grows as in the continuum case, and yet, simultaneously, the spike side of the interface exhibits planar density contours as in the case of rarefied regime. This is unexpected, since at the high Atwood number considered here ($A = 0.8$), classical RTI exhibits much faster growth on the spike side. To explain the observed behavior, metrics that quantify the effects of advection, diffusion, and pressure effects are developed. It is then demonstrated that in the continuum regime, the advective phenomenon drives the dynamics on either side of the interface. As expected, in the fully rarefied regime, diffusive effects determine the evolution. In the intermediate regime, advective effects dominate on the bubble side, while the diffusive effects are more prominent on the other side. This advective–diffusive asymmetry leads to significant differences in the manner of the density front evolution on the two sides of the interface. The Knudsen–Mach number parameter range of the occurrence of the advective–diffusive asymmetry is established. Future work will focus on characterizing the RTI at higher Mach and Knudsen numbers using the unified gas kinetic scheme.

ACKNOWLEDGMENTS

This work was performed under the auspices of DOE. S.M. and S.S.G. have been supported through Triad award 628660. LANL, an affirmative action/equal opportunity employer, is managed by Triad National Security, LLC, for the National Nuclear Security Administration of the U.S. Department of Energy under contract 89233218CNA000001.

AUTHOR DECLARATIONS

Conflict of Interest

The authors have no conflicts to disclose.

Author Contributions

Swapnil Majumder: Data curation (equal); Formal analysis (equal); Writing – original draft (equal). **Daniel Livescu:** Conceptualization (equal); Formal analysis (equal); Writing – review & editing (equal). **Sharath S. Girimaji:** Conceptualization (equal); Formal analysis (equal); Writing – review & editing (equal).

DATA AVAILABILITY

The data that support the findings are available from the corresponding author upon reasonable request.

REFERENCES

[1]L. Rayleigh, "Investigation of the character of the equilibrium of an incompressible heavy fluid of variable density," Proc. London Math. Soc. **1**, 170–177 (1882).
[2]G. I. Taylor, "The instability of liquid surfaces when accelerated in a direction perpendicular to their planes. I," Proc. R. Soc. London. Ser. A **201**, 192–196 (1950).
[3]M. Zingale, S. E. Woosley, C. A. Rendleman, M. S. Day, and J. B. Bell, "Three-dimensional numerical simulations of Rayleigh-Taylor unstable flames in type Ia supernovae," Astrophys. J. **632**, 1021 (2005).
[4]A. G. Nouri, P. Givi, and D. Livescu, "Modeling and simulation of turbulent nuclear flames in type Ia supernovae," Prog. Aerosp. Sci. **108**, 156–179 (2019).
[5]R. S. Craxton, K. S. Anderson, T. R. Boehly, V. N. Goncharov, D. R. Harding, J. P. Knauer, R. L. McCrory, P. W. McKenty, D. D. Meyerhofer, J. F. Myatt, A. J. Schmitt, J. D. Sethian, R. W. Short, S. Skupsky, W. Theobald, W. L. Kruer, K. Tanaka, R. Betti, T. J. B. Collins, J. A. Delettrez, S. X. Hu, J. A. Marozas, A. V. Maximov, D. T. Michel, P. B. Radha, S. P. Regan, T. C. Sangster, W. Seka, A. A. Solodov, J. M. Soures, C. Stoeckl, and J. D. Zuegel, "Direct-drive inertial confinement fusion: A review," Phys. Plasmas **22**, 110501 (2015).
[6]R. Betti, V. N. Goncharov, R. L. McCrory, and P. C. Verdon, "Growth rates of the ablative Rayleigh–Taylor instability in inertial confinement fusion," Phys. Plasmas **5**, 1446–1454 (1998).
[7]T. Wei and D. Livescu, "Late-time quadratic growth in single-mode Rayleigh-Taylor instability," Phys. Rev. E **86**, 046405 (2012).
[8]X. Bian, H. Aluie, D. Zhao, H. Zhang, and D. Livescu, "Revisiting the late-time growth of single-mode Rayleigh–Taylor instability and the role of vorticity," Phys. D **403**, 132250 (2020).
[9]S. Weiland, P. E. Hamlington, S. J. Reckinger, and D. Livescu, "Effects of isothermal stratification strength on vorticity dynamics for single-mode compressible Rayleigh-Taylor instability," Phys. Rev. Fluids **4**, 093905 (2019).
[10]S. Weiland, S. J. Reckinger, P. E. Hamlington, and D. Livescu, "Effects of background stratification on the compressible Rayleigh Taylor instability," in *AIAA Aviation Forum 2017* (AIAA, 2017), pp. 2017–3974.
[11]S. Majumder, B. Sharma, D. Livescu, and S. Girimaji, "Compressible Rayleigh–Taylor instability subject to isochoric initial background state," Phys. Fluids **35**, 094113 (2023).
[12]I. Sagert, J. Howell, A. Staber, T. Strother, D. Colbry, and W. Bauer, "Knudsen-number dependence of two-dimensional single-mode Rayleigh-Taylor fluid instabilities," Phys. Rev. E **92**, 013009 (2015).
[13]Z. Guang, Z. Chengwen, L. Sha, W. Yong, and Z. Congshan, "Application of gas-kinetic scheme for continuum and near-continuum flow on unstructured mesh," Int. J. Comput. Fluid Dyn. **36**, 753–775 (2022).
[14]V. Mohan, A. Sameen, B. Srinivasan, and S. S. Girimaji, "Influence of Knudsen and Mach numbers on Kelvin-Helmholtz instability," Phys. Rev. E **103**, 053104 (2021).
[15]V. Venugopal, D. S. Praturi, and S. S. Girimaji, "Non-equilibrium thermal transport and entropy analyses in rarefied cavity flows," J. Fluid Mech. **864**, 995–1025 (2019).
[16]K. Xu and J. Huang, "A unified gas-kinetic scheme for continuum and rarefied flows," J. Comput. Phys. **229**, 7747–7764 (2010).
[17]J. Huang, K. Xu, and P. Yu, "A unified gas-kinetic scheme for continuum and rarefied flows ii: Multi-dimensional cases," Comm. Comput. Phys. **12**, 662–690 (2012).
[18]D. Livescu, "Compressibility effects on the Rayleigh–Taylor instability growth between immiscible fluids," Phys. Fluids **16**, 118–127 (2004).
[19]K. Xu, "Gas-kinetic schemes for unsteady compressible flow simulations," in *29th* Computational Fluid Dynamics, Annual Lecture Series (1998).
[20]A. Manela and I. Frankel, "On the compressible Taylor–Couette problem," J. Fluid Mech. **588**, 59–74 (2007).
[21]A. Manela and J. Zhang, "The effect of compressibility on the stability of wall-bounded Kolmogorov flow," J. Fluid Mech. **694**, 29–49 (2012).
[22]S. Stefanov, V. Roussinov, and C. Cercignani, "Rayleigh–Bénard flow of a rarefied gas and its attractors. I. Convection regime," Phys. Fluids **14**, 2255–2269 (2002).
[23]A. Manela and I. Frankel, "On the Rayleigh–Bénard problem in the continuum limit," Phys. Fluids **17**, 036101 (2005).
[24]Y. Ben-Ami and A. Manela, "Effect of heat-flux boundary conditions on the Rayleigh-Bénard instability in a rarefied gas," Phys. Rev. Fluids **4**, 033402 (2019).

[25]K. Xu, "A gas-kinetic BGK scheme for the Navier-Stokes equations and its connection with artificial dissipation and Godunov method," J. Comput. Phys. **171**, 289–335 (2001).
[26]K. Xu, M. Mao, and L. Tang, "A multidimensional gas-kinetic BGK scheme for hypersonic viscous flow," J. Comput. Phys. **203**, 405–421 (2005).
[27]K. Xu, L. Martinelli, and A. Jameson, "Gas-kinetic finite volume methods, flux-vector splitting, and artificial diffusion," J. Comput. Phys. **120**, 48–65 (1995).
[28]P. L. Bhatnagar, E. P. Gross, and M. Krook, "A model for collision processes in gases. I. Small amplitude processes in charged and neutral one-component systems," Phys. Rev. **94**, 511–525 (1954).
[29]G. Kumar, S. S. Girimaji, and J. Kerimo, "Weno-enhanced gas-kinetic scheme for direct simulations of compressible transition and turbulence," J. Comput. Phys. **234**, 499–523 (2013).
[30]T. Poinsot and S. Lele, "Boundary conditions for direct simulations of compressible viscous flows," J. Comput. Phys. **101**, 104–129 (1992).
[31]S. J. Reckinger, D. Livescu, and O. V. Vasilyev, "Comprehensive numerical methodology for direct numerical simulations of compressible Rayleigh–Taylor instability," J. Comput. Phys. **313**, 181–208 (2016).
[32]D. Livescu, T. Wei, and P. Brady, "Rayleigh–Taylor instability with gravity reversal," Phys. D **417**, 132832 (2021).